LETTERS
PUBLISHED ONLINE: 1 JUNE 2015 | DOI: 10.1038/NCLIMATE2658
nature climate change

Projected strengthening of Amazonian dry season by constrained climate model simulations

Juan P. Boisier[1*†], Philippe Ciais[2], Agnès Ducharne[1] and Matthieu Guimberteau[1,2]

The vulnerability of Amazonian rainforest, and the ecological services it provides, depends on an adequate supply of dry-season water, either as precipitation or stored soil moisture. How the rain-bearing South American monsoon will evolve across the twenty-first century is thus a question of major interest. Extensive savanization, with its loss of forest carbon stock and uptake capacity, is an extreme although very uncertain scenario[1–6]. We show that the contrasting rainfall projections simulated for Amazonia by 36 global climate models (GCMs) can be reproduced with empirical precipitation models, calibrated with historical GCM data as functions of the large-scale circulation. A set of these simple models was therefore calibrated with observations and used to constrain the GCM simulations. In agreement with the current hydrologic trends[7,8], the resulting projection towards the end of the twenty-first century is for a strengthening of the monsoon seasonal cycle, and a dry-season lengthening in southern Amazonia. With this approach, the increase in the area subjected to lengthy—savannah-prone—dry seasons is substantially larger than the GCM-simulated one. Our results confirm the dominant picture shown by the state-of-the-art GCMs, but suggest that the 'model democracy' view of these impacts can be significantly underestimated.

Reducing the large uncertainties of the regional precipitation response to anthropogenic climate forcing (ACF) is a crucial challenge in the assessment of the future climate and water resources availability[9]. Even though the main mechanisms driving the large-scale changes in precipitation simulated by GCMs are known[10–16], a convergence of the model projections is not expected in the near term[17]. The ACF impacts on the South American monsoon[18] (SAM) are particularly interesting given the local and global implications of changes in the functioning of Amazonian rainforest[1–8,19]. However, even state-of-the-art GCMs are poor at simulating the mean rainfall regime and its variability over tropical South America[20,21], and the projections remain notoriously uncertain in this region[9,21–23].

The changes in the Amazonian precipitation (P_A) are addressed here using both an observational data set and an ensemble of simulations from 36 GCMs participating in phase 5 of the Coupled Model Intercomparison Project (CMIP5). The model data combine transient historical simulations from 1960 to 2005 and twenty-first century projections under a high-emission scenario (RCP8.5, see Methods and Supplementary Information).

An overview of the CMIP5 model outputs illustrates the uncertainties in the projected P_A (Fig. 1a). Across the twenty-first century, the ensemble of GCMs shows a slightly negative trend in basin-wide mean annual P_A embedded in a large inter-model spread, with nearly half of the models showing a trend towards wetter conditions. The CMIP5 ensemble also indicates a strengthening of the SAM annual cycle by the end of the twenty-first century (Fig. 2e), characterized by a late-dry-season rainfall decrease (-0.54 ± 0.63 mm d^{-1} in September–November (SON)), and a slightly wetter wet season (December–February (DJF)). Yet, this pattern of change is not systematic among the GCMs assessed, and ~20% of them simulate a decrease of the SAM amplitude in response to ACF (not shown).

Qualitatively, the uncertainty in the regional precipitation responses to ACF can be attributed to different processes operating within GCMs at different scales (Fig. 1b), ranging from the global climate sensitivity to CO_2 concentration increase—and underlying changes in large-scale temperature, moisture, circulation and precipitation[24,25]—to regional-scale impacts driven by other factors, for example, land-use change[26]. The way the large-scale perturbations affect a region, such as Amazonia, constitutes another particularly interesting source of uncertainty. The GCM discrepancies refer, in this case, to model-specific sensitivities in mesoscale circulation and rainfall to phenomena such as El Niño/Southern Oscillation[21], or to changes in land–ocean temperature contrast (see Supplementary Fig. 3).

To investigate the processes governing the P_A projections in GCMs, we first looked at the simulated long-term changes in moisture flux convergence in Amazonia ($-\nabla \cdot \mathbf{Q}_A$) and at two components of this variable driven by moisture and circulation perturbations (Methods). We found a close inter-model relationship between the changes in P_A and $-\nabla \cdot Q_A$ simulated at the end of the twenty-first century, indicating that atmospheric processes play a leading role in the control of precipitation responses to ACF (Fig. 1c). This relationship, however, cannot be explained without the atmospheric circulation anomalies. The tropospheric warming and concurrent increase in water vapour content produces an almost systematic increase in moisture convergence (Fig. 1d)—a thermodynamic effect consistent with the convective regime in place across the Amazon Basin during most of the year (that is, the so-called wet-get-wetter response). In contrast, a major dynamic influence on the P_A changes is observed across the GCMs (Fig. 1e), consistent with other studies pointing out circulation as a strong control of regional patterns of precipitation change[15,16], and as a major uncertainty source in the modelled response to ACF (refs 16,25).

Following a variety of recent studies using observational benchmarks for climate simulations[19,27,28], we build here an empirical relationship between observed P_A and large-scale circulation indicators to provide a constraint on GCM projections. The approach resembles statistical downscaling, as it relates mesoscale (~200 km) patterns of precipitation within the Amazon Basin with explanatory variables at a larger scale (~2,000 km).

[1]UMR 7619 METIS, IPSL, Sorbonne Universités, UPMC, CNRS, EPHE, 75252 Paris, France. [2]Laboratoire des Sciences du Climat et de l'Environnement, IPSL, CEA, CNRS, UVSQ, 91191 Gif-sur-Yvette, France. †Present address: Department of Geophysics, Universidad de Chile, and Center for Climate and Resilience Research (CR)[2], Santiago 8370449, Chile. *e-mail: jboisier@dgf.uchile.cl

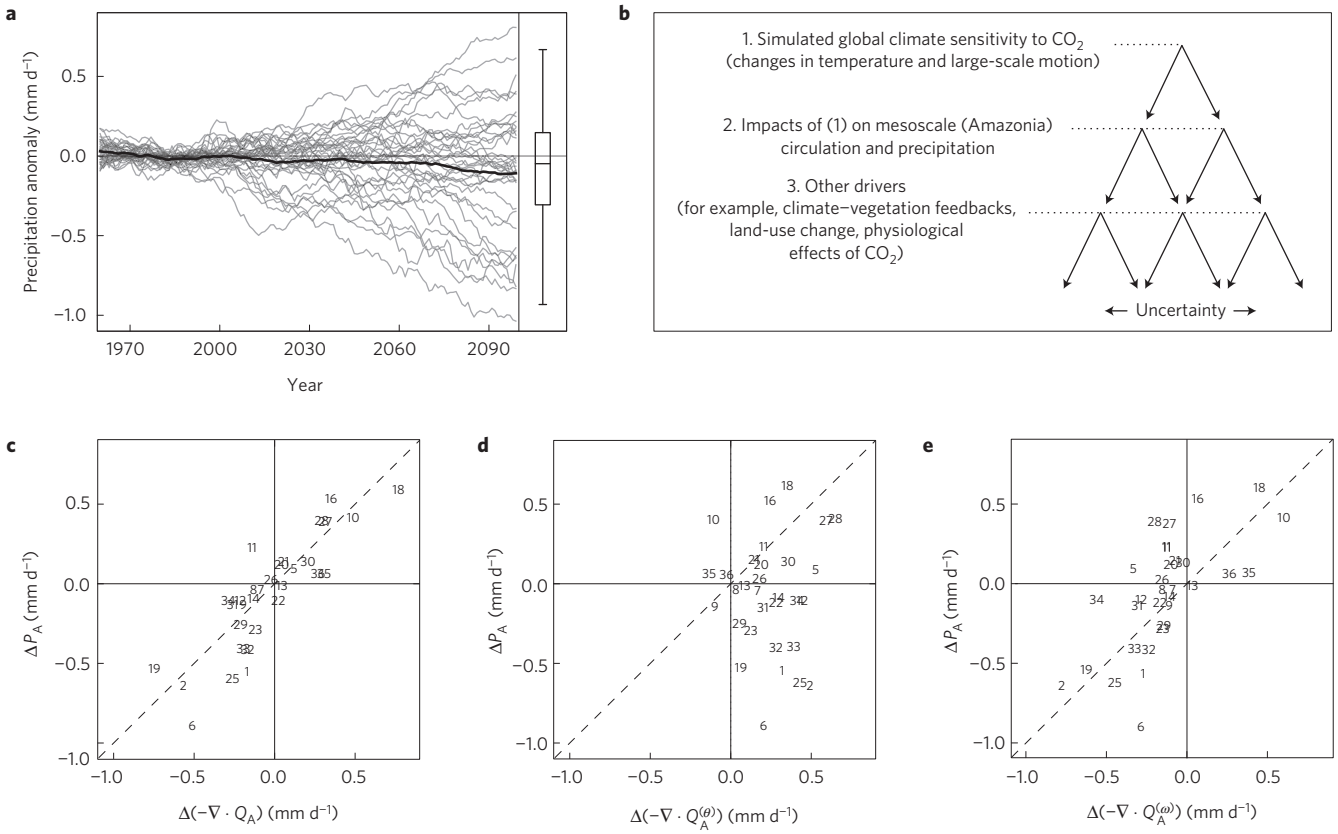

Figure 1 | Simulated changes in Amazonian precipitation. a, Annual mean precipitation anomalies (relative to 1960–1999) simulated in Amazonia (P_A, basin-wide mean) by 36 CMIP5 GCMs (time series smoothed with an 11-year running mean filter). Box–whisker plot indicates the ensemble median, lower/upper quartiles and extremes in 2070–2099. **b**, Qualitative outline of the sources of uncertainty in the projected P_A. Given a socioeconomic scenario, a first discrepancy between GCMs relies on the global-scale climate sensitivity to the anthropogenic climate forcing. The way the large-scale perturbations affect Amazonia represents another source of uncertainty of particular interest in this study. Regional impacts driven by land-surface processes are combined into a third source of uncertainty (including, for example, feedbacks between vegetation and regional climate, physiological effects of CO_2 on plant transpiration, or land-use change). **c**, Difference in annual P_A between the ends of the twentieth (1960–1999) and twenty-first (2060–2099) centuries (ΔP_A), plotted against the corresponding difference in water vapour flux convergence ($\Delta(-\nabla \cdot Q_A)$). Numbers indicate the various GCMs assessed (Supplementary Table 1). **d**,**e**, The same as in **c**, but for the thermodynamic and the dynamic component of $\mathbf{Q}_A$ ($\mathbf{Q}_A^{(\theta)}$ and $\mathbf{Q}_A^{(\omega)}$, respectively; see Methods).

The method followed relies on regression models of P_A calibrated against historical observations (1960–2012) of precipitation and sea-level pressure (p_{SL}). These models aim to mimic the leading modes of rainfall variability observed across the basin as functions of p_{SL} of different regions of the globe (Methods). A large ensemble of constrained P_A projections is finally computed by forcing the regression models with the p_{SL} data simulated by each CMIP5 GCM from 1960 to 2099 (Supplementary Fig. 4).

We note that the empirical models constructed can account only for the large-scale influence on P_A; many other processes are thus ignored (Fig. 1b). The method also assumes a simple dependency of P_A on the p_{SL} predictors, and that the relationship established for the present-day period will hold true in a future climate. To validate our approach, we computed another set of models using for calibration the historical precipitation and p_{SL} simulated by each GCM. The similarity between the P_A change simulated by a given GCM and the corresponding statistical (GCM-based) P_A projections allows us to assess the capacity of the empirical models to predict the future evolution of P_A (Supplementary Information).

Considering the important caveats mentioned above, the predictive skill shown by the empirical models is fairly good. The statistical reconstructions explain most of the historical P_A variability and predict, in most cases, the future changes simulated by the GCMs (Fig. 2c,f and Supplementary Figs 5–7). Given these results, and aware of the limitations of the validation procedure (see Supplementary Information), we consider it pertinent to go through the P_A projections analysis using the empirical models calibrated with observations. This 'diagnostic' ensemble reasserts the general picture shown by the CMIP5 ensemble (Fig. 2g): a marked rainfall decline is projected to the end of the twenty-first century in the late dry season (-0.58 ± 0.39 mm d^{-1} in SON; a deficit of 14%), whereas a moderate P_A increase is diagnosed in the wet season. However, compared with the GCM simulations, the constrained projections show a drying signal appearing earlier in the dry season, resulting in a stronger overall impact during that season.

The spatial distribution of the P_A changes shows a clearer difference between the simulated and constrained projections (Fig. 3). The GCMs show, on average, large precipitation increases in the eastern tropical Pacific affecting the western bounds of the Amazon Basin in DJF and March–May (MAM; Fig. 3a). The late-dry-season (SON) drying affects most of the Amazon Basin but is particularly strong in the northeast of the region. A different picture is obtained with the constrained projections, which show a widespread drying both in June–August (JJA) and SON, and a larger sign concordance across the individual estimates compared with the GCM simulations (Fig. 3b). The drying signal in SON principally affects the southern part of the basin. In that region, the strong rainfall seasonality and water limitation during the dry season makes the rainforest particularly vulnerable to persistent soil moisture deficits[2]. We therefore follow a similar approach to earlier

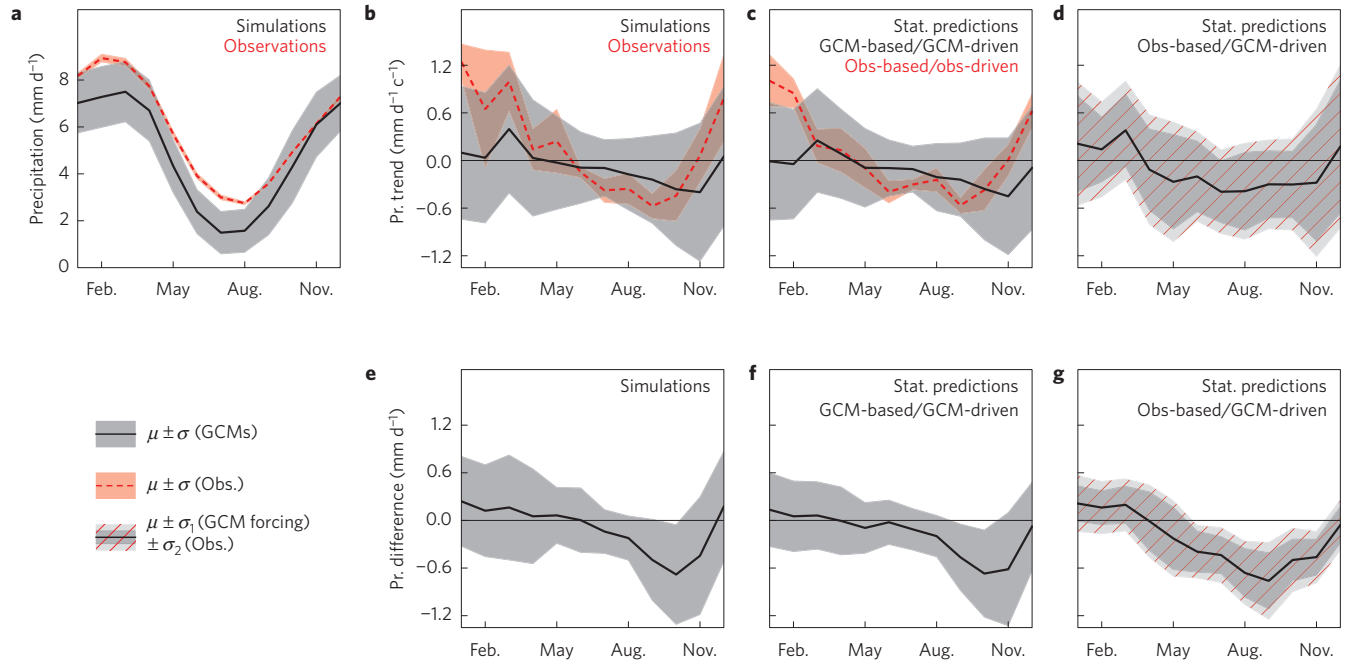

Figure 2 | Amazonian precipitation climatology, trends and long-term changes. a, Present-day (1960–1999) monthly mean precipitation in Amazonia (P_A, basin-wide mean). **b**–**d**, Linear trends of P_A from 1960 to 2010. **e**–**g**, P_A change between the ends of the twentieth (1960–1999) and twenty-first (2060–2099) centuries. Thick lines and envelopes in **a**,**b** and **e** indicate the ensemble averages (μ) ± 1.0 s.d. (σ) derived from the CMIP5 simulations (black) and from observational data (red-dashed; Methods). **c**,**f**, Statistical predictions based on the regression models calibrated with GCMs (used for control and evaluation; see Supplementary Fig. 4) are shown in black lines and grey envelopes. **d**,**g**, Statistical predictions based on the regression models calibrated with observations (constrained projections). Light grey intervals indicate the fraction of σ associated with differences in the observational data sets.

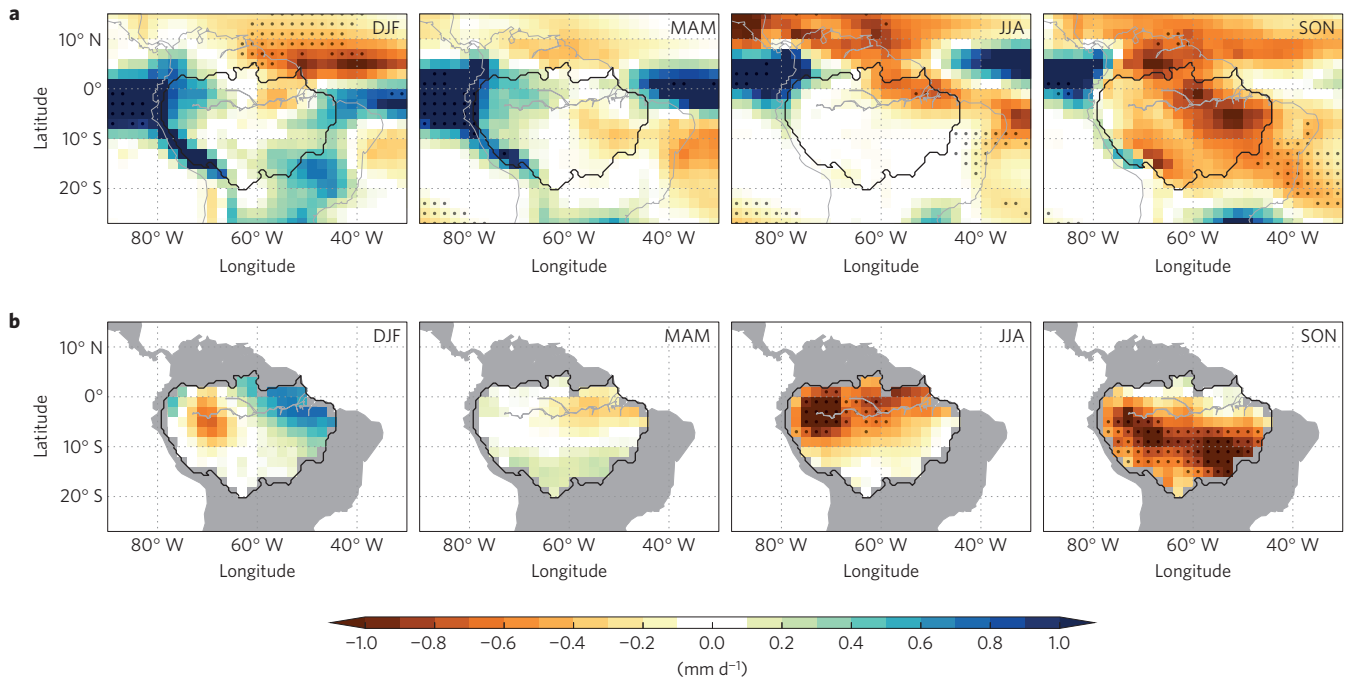

Figure 3 | Simulated and constrained projections. a,**b**, Seasonal and ensemble mean precipitation difference between the ends of the twentieth (1960–1999) and twenty-first (2060–2099) centuries simulated by the CMIP5 GCMs (**a**) and diagnosed, based on the constrained projections (**b**). Dots indicate grid cells in which more that 90% of the corresponding ensemble members agree in sign.

studies[3,4] and assess future Amazon rainforest resilience against the P_A projections derived here.

The dry-season length (DSL, Methods) is a simple indicator of seasonal rainfall regimes and a straightforward constraint for tropical biomes[5]. The present-day precipitation and land-cover condition[29] show that indeed rainforest is the clear dominant biome in tropical regions with a DSL of less than three months (Fig. 4a). Above this limit, forest prevalence decreases sharply, and there is

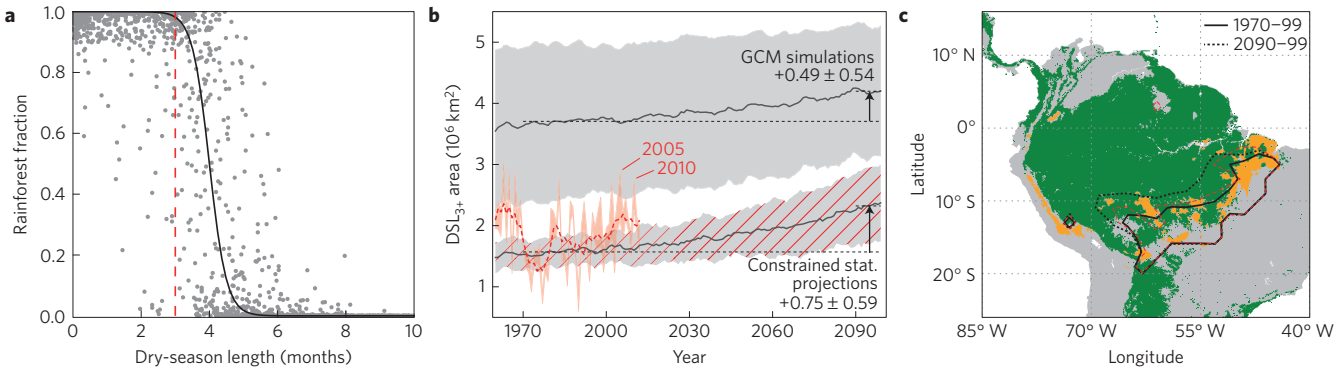

Figure 4 | Projected changes in Amazonian dry season and potential impacts on rainforest. a, Areal fraction of tropical (25° S–25° N) rainforest plotted against the mean (1980–2010) dry-season length (DSL; Methods), based on the MODIS land cover[29] and the GPCC precipitation data set at 1.0° of resolution. Grid cells with human-made (cropland, urban) or/and wetland fraction above 5% were excluded from analysis. **b**, Observed (red-dashed line), simulated (CMIP5, black line and grey shading) and diagnosed (observations-constrained; black line, grey shading and red hatches) yearly area within the Amazon Basin with DSL above 3 months (DSL_{3+}). Ensemble means (μ, thick lines) and standard deviations (σ, shading indicates $\mu \pm 1.0\sigma$) are calculated from filtered time series (5-year running mean). Red envelope illustrates $\mu \pm 1.0\sigma$ computed with the non-filtered observational data. **c**, Amazonian DSL_{3+} area derived from the observed (GPCC, dashed red) and diagnosed (solid black) present-day precipitation (1970–1999). The dotted black contour indicates the DSL_{3+} area diagnosed on average in 2090–2099. Green and orange pixels indicate regions with dominating fraction (>50%) of forest and deforested area, respectively.

a relatively narrow DSL domain where forests can cohabit with savannahs and treeless biomes. Hence, we use a DSL threshold of three months to define a rainfall regime (DSL_{3+}) and regions where pre-existing rainforests are susceptible to switching to other biomes.

Within the Amazon Basin, the observed precipitation defines an area satisfying DSL_{3+} of 1.8 million km^2, including southeastern Amazonia and the Brazilian Cerrado (Fig. 4b,c). Yet, there is large spread on the DSL_{3+} area derived from the historical GCM simulations (ranging from 1.3 to 6.2 million km^2). Further, the simulated mean value of this metric is about twice as large as the one observed (Fig. 4b). This bias and uncertainty illustrates the difficulty in assessing correctly the potential climate-change effects on the Amazonian ecosystem based on the current GCM simulations. In contrast, the diagnosed P_A defines a DSL_{3+} domain that is consistent with the observations (Fig. 4b,c).

Both the constrained and GCM projections indicate an expansion of the DSL_{3+} area (Fig. 4b), but the diagnosed increase of this area by the end of the twenty-first century (of +0.75 million km^2 on average) is substantially larger than the GCM-simulated one (+0.5 million km^2). We note that the uncertainties in the constrained projections remain large, even though they show a stronger signal-to-noise ratio than the CMIP5 ensemble (Figs 2g and 4b). These uncertainties respond mainly to the imposed large-scale p_{SL} forcing and, less so, to differences within the various observational data sets used and to noise induced by natural variability (see Fig. 2g and Methods).

In summary, our study suggests an important underestimation of the ACF impacts on Amazonian precipitation as simulated by the CMIP5 GCMs. The dry biases in this region, common in the models (Fig. 2a), may be a key reason for the future impact underestimation, because GCMs already showing very dry present-day conditions cannot undergo a severe reduction in precipitation. As in the long-term projections, the historical P_A trends seem underestimated in the CMIP5 ensemble. Compared with the observations, the rainfall trends simulated between 1960 and 2010 show a coherent seasonality, but a weaker amplitude (Fig. 2b). Consistent with the findings in ref. 8, the observation-based P_A trends are even larger if we consider a shorter (satellite-observed) period (Supplementary Fig. 2). A concomitant expansion of the Amazonian DSL_{3+} area of 0.88 million km^2 per century is observed between 1980 and 2012, notably influenced by the widespread droughts of 2005 and 2010 (Fig. 4b). Yet, although large compared with the long-term projections, this trend should be interpreted with care because it does not emerge clearly from the large interannual variability (p value > 0.05).

In our view, the technique developed here makes best use of the available observations from the region, while still harnessing the scientific knowledge inherent in an ensemble of GCM simulations. This pragmatic approach should produce more accurate projections. We thus argue that the rainforest decline is a likely response to future rainfall changes in southern Amazonia. Our estimates do not account for feedbacks from land surface nor changes in water recycling. This area is also under the direct pressure of deforestation (Fig. 4c), so the overarching question remains whether the combined impacts of climate and land-use change could trigger a widespread forest dieback, and how these two drivers may interact.

Methods

Methods and any associated references are available in the online version of the paper.

Received 6 November 2014; accepted 17 April 2015; published online 1 June 2015

References

1. Cox, P. M. *et al.* Amazonian forest dieback under climate-carbon cycle projections for the 21st century. *Theor. Appl. Climatol.* **78,** 137–156 (2004).
2. Hirota, M., Holmgren, M., Nes, E. H. V. & Scheffer, M. Global resilience of tropical forest and savanna to critical transitions. *Science* **334,** 232–235 (2011).
3. Zeng, Z. *et al.* Committed changes in tropical tree cover under the projected 21st century climate change. *Sci. Rep.* **3,** 1951 (2013).
4. Malhi, Y. *et al.* Exploring the likelihood and mechanism of a climate-change-induced dieback of the Amazon rainforest. *Proc. Natl Acad. Sci. USA* **106,** 20610–20615 (2009).
5. Good, P., Jones, C., Lowe, J., Betts, R. & Gedney, N. Comparing tropical forest projections from two generations of Hadley Centre Earth System Models, HadGEM2-ES and HadCM3LC. *J. Clim.* **26,** 495–511 (2013).
6. Huntingford, C. *et al.* Simulated resilience of tropical rainforests to CO_2-induced climate change. *Nature Geosci.* **6,** 268–273 (2013).
7. Marengo, J. A., Tomasella, J., Alves, L. M., Soares, W. R. & Rodriguez, D. A. The drought of 2010 in the context of historical droughts in the Amazon region. *Geophys. Res. Lett.* **38,** L12703 (2011).
8. Fu, R. *et al.* Increased dry-season length over southern Amazonia in recent decades and its implication for future climate projection. *Proc. Natl Acad. Sci. USA* **110,** 18110–18115 (2013).
9. Collins, M. *et al.* in *IPCC Climate Change 2013: The Physical Science Basis* (eds Stocker, T. F. *et al.*) Ch. 12, 1029–1136 (IPCC, Cambridge Univ. Press, 2013).

10. Held, I. M. & Soden, B. J. Robust responses of the hydrological cycle to global warming. *J. Clim.* **19,** 5686–5699 (2006).
11. Chou, C., Neelin, J. D., Chen, C-A. & Tu, J-Y. Evaluating the Rich-Get-Richer mechanism in tropical precipitation change under global warming. *J. Clim.* **22,** 1982–2005 (2009).
12. Seager, R., Naik, N. & Vecchi, G. A. Thermodynamic and dynamic mechanisms for large-scale changes in the hydrological cycle in response to global warming. *J. Clim.* **23,** 4651–4668 (2010).
13. Muller, C. J. & O'Gorman, P. A. An energetic perspective on the regional response of precipitation to climate change. *Nature Clim. Change* **1,** 266–271 (2011).
14. Huang, P., Xie, S-P., Hu, K., Huang, G. & Huang, R. Patterns of the seasonal response of tropical rainfall to global warming. *Nature Geosci.* **6,** 357–361 (2013).
15. Chadwick, R., Boutle, I. & Martin, G. Spatial patterns of precipitation change in CMIP5: Why the rich do not get richer in the tropics. *J. Clim.* **26,** 3803–3822 (2013).
16. Bony, S. *et al.* Robust direct effect of carbon dioxide on tropical circulation and regional precipitation. *Nature Geosci.* **6,** 447–451 (2013).
17. Knutti, R. & Sedlek, J. Robustness and uncertainties in the new CMIP5 climate model projections. *Nature Clim. Change* **3,** 369–373 (2013).
18. Vera, C. *et al.* Toward a unified view of the American monsoon systems. *J. Clim.* **19,** 4977–5000 (2006).
19. Cox, P. M. *et al.* Sensitivity of tropical carbon to climate change constrained by carbon dioxide variability. *Nature* **494,** 341–344 (2013).
20. Yin, L., Fu, R., Shevliakova, E. & Dickinson, R. E. How well can CMIP5 simulate precipitation and its controlling processes over tropical South America? *Clim. Dynam.* **41,** 3127–3143 (2013).
21. Joetzjer, E., Douville, H., Delire, C. & Ciais, P. Present-day and future Amazonian precipitation in global climate models: CMIP5 versus CMIP3. *Clim. Dynam.* **41,** 2921–2936 (2013).
22. Li, W., Fu, R. & Dickinson, R. E. Rainfall and its seasonality over the Amazon in the 21st century as assessed by the coupled models for the IPCC AR4. *J. Geophys. Res.* **111,** D02111 (2006).
23. Seth, A., Rojas, M. & Rauscher, S. A. CMIP3 projected changes in the annual cycle of the South American Monsoon. *Climatic Change* **98,** 331–357 (2010).
24. Stevens, B. & Bony, S. What are climate models missing? *Science* **340,** 1053–1054 (2013).
25. Shepherd, T. G. Atmospheric circulation as a source of uncertainty in climate change projections. *Nature Geosci.* **7,** 703–708 (2014).
26. Brovkin, V. *et al.* Effect of anthropogenic land-use and land-cover changes on climate and land carbon storage in CMIP5 projections for the twenty-first century. *J. Clim.* **26,** 6859–6881 (2013).
27. Hall, A. & Qu, X. Using the current seasonal cycle to constrain snow albedo feedback in future climate change. *Geophys. Res. Lett.* **33,** L03502 (2006).
28. Shiogama, H. *et al.* Observational constraints indicate risk of drying in the Amazon basin. *Nature Commun.* **2,** 253 (2011).
29. Friedl, M. A. *et al.* MODIS Collection 5 global land cover: Algorithm refinements and characterization of new datasets. *Remote Sens. Environ.* **114,** 168–182 (2010).

Acknowledgements

This research received financial support from the European Union Seventh Framework Programme, under the project AMAZALERT (Grant Agreement No. 282664). J.P.B. is grateful for support from the CONICYT (Chile) grants FONDAP (Center for Climate and Resilience Research, No. 15110009) and FONDECYT (No. 3150492). We acknowledge the World Climate Research Programme's Working Group on Coupled Modelling, which is responsible for CMIP, and we thank the climate modelling groups (listed in Supplementary Table 1 of this paper) for producing and making available their model output. For CMIP the US Department of Energy's Program for Climate Model Diagnosis and Intercomparison provides coordinating support and led development of software infrastructure in partnership with the Global Organization for Earth System Science Portals. The precipitation data used in this paper were extracted from publicly available sites and are described, with references, in the supporting material. The MODIS MCD12C1 product was obtained through the online Data Pool at the NASA Land Processes Distributed Active Archive Center (LP DAAC), USGS/Earth Resources Observation and Science (EROS) Center, Sioux Falls, South Dakota (https://lpdaac.usgs.gov/data_access).

Author contributions

J.P.B. designed the study and conducted the analysis. All authors advised on the approach followed, interpreted the results and contributed to the manuscript preparation.

Additional information

Supplementary information is available in the online version of the paper. Reprints and permissions information is available online at www.nature.com/reprints. Correspondence and requests for materials should be addressed to J.P.B.

Competing financial interests

The authors declare no competing financial interests.

Methods

Model and observational data. We used monthly data from transient coupled simulations carried out with 36 GCMs participating in CMIP5 (Supplementary Table 1). The whole period analysed spans from 1960 to 2099, including a single historical run (1960–2005) per model and the corresponding twenty-first century projection (2006–2099) following Representative Concentration Pathway 8.5 (RCP8.5, see Supplementary Information).

In addition to precipitation and sea-level pressure (p_{SL}), we used three-dimensional wind ($\mathbf{u}=\{u,v\}$) and specific humidity (q) data for the computation of a vertically integrated water vapour flux ($\mathbf{Q}$), which is derived as:

$$\mathbf{Q}=g_0^{-1}\int_{p_T}^{p_S} q\,\mathbf{u}\,dp \quad (1)$$

where g_0 and p_S are the gravitational acceleration and pressure at the surface, respectively. The top pressure level p_T is set to 100 hPa. A dynamic ($\mathbf{Q}^{(\omega)}$) and a thermodynamic ($\mathbf{Q}^{(\theta)}$) component of $\mathbf{Q}$ are derived as in equation (1), but prescribing the climatological mean (1960–1999) profiles of q ($\overline{q}$) and $\mathbf{u}$ ($\overline{\mathbf{u}}$), respectively:

$$\mathbf{Q}^{(\omega)}=g_0^{-1}\int_{p_T}^{p_S} \overline{q}\,\mathbf{u}\,dp \quad (2)$$

$$\mathbf{Q}^{(\theta)}=g_0^{-1}\int_{p_T}^{p_S} q\,\overline{\mathbf{u}}\,dp \quad (3)$$

We use a trapezoidal rule to estimate the vertical integrals in the equations (1)–(3) from the pressure levels available in the GCMs' atmospheric fields. The water vapour flux divergence terms ($\nabla\cdot\mathbf{Q}$, $\nabla\cdot\mathbf{Q}^{(\omega)}$ and $\nabla\cdot\mathbf{Q}^{(\theta)}$) further used for the analysis depicted in Fig. 1 were computed using central finite-difference approximations in spherical coordinates.

The observational data set includes four gridded products of land precipitation from the Global Precipitation Climatology Centre (GPCC), the National Centers for Environmental Prediction (PREC/L), the Climatic Research Unit (CRU) and from the University of Delaware (UDEL). The monthly data from the Hadley Centre Sea Level Pressure data set[30] (HadSLP2) were adopted for p_{SL}. Further details, references, and an evaluation of these products are provided as Supplementary Information.

The Amazon Basin-wide average of a given variable is calculated as the spatial area-weighted mean over a region of ~7 million km^2 (Fig. 3). To have a consistent domain within the multiple GCM and observational data sets, all fields were previously interpolated and analysed in a common rectangular grid of 2.0° latitude–longitude.

The P_A responses to ACF are derived as differences between climatologies computed at the end of the twentieth (1960–1999) and twenty-first (2060–2099) centuries. We note that part of these differences could be affected by multi-decadal internal variability simulated in GCMs. The noise induced by these stochastic variations is offset when averages are applied to ensembles (see, for example, Fig. 2), but the standard deviation values should partially reflect uncertainties due to variability.

The dry-season length (DSL) is defined as the number of months per year with precipitation rates below 2 mm d^{-1}. A minimum DSL of three months is used to define a rainfall regime (DSL_{3+}) where savannahs/treeless biomes prevail and, therefore, where rainforest is less resilient to permanent changes in precipitation. Vulnerable areas within the Amazonian domain are computed yearly with the pixels satisfying DSL_{3+}. The present-day vegetation partitioning is based on the MODIS land-cover product MCD12C1 (ref. 29) averaged from 2001 to 2010. We note the manifest problem of using monthly precipitation data to properly define dry seasons. However, for the purpose of this study, this disadvantage has a lesser impact because we compute time averages and regional statistics to derive, respectively, DSL climatologies (from which fractional values are obtained, Fig. 4a) and yearly DSL_{3+} areas (Fig. 4b).

Empirical models of Amazonian precipitation. A multivariate regression analysis was performed to derive the link between patterns of precipitation in Amazonia and p_{SL} of different regions of the globe. The choice of p_{SL} as an indicator of the large-scale motion relies in part on the availability of historical reconstructions of good quality[30]. The analysis accounts for the rainfall distribution across the basin. For this purpose, the leading modes of variability were extracted using a standard empirical orthogonal function decomposition. This approach allows us to describe the spatiotemporal variability of P_A with only a few time series (we used the first 10 principal components), hence avoiding multiple analyses at the pixel level. This approach also ensures a spatial coherency on the reconstructed P_A fields.

Several regression models were derived with the historical data (1960–2012) both from the observational products (used to compute the constrained rainfall projections) and from the GCM simulations (used for the method evaluation; see Supplementary Fig. 4). The analysis was done separately for each month of the year. However, information from the months preceding and following the one assessed was also included in the calibrating data, allowing us to increase by a factor of 3 the record length used in the analyses, thereby providing robustness in regression-parameter computation. Hence, both the interannual variability and a small part of the seasonal cycle are accounted for in the models' calibration.

The explanatory variables correspond to normalized monthly p_{SL} anomalies averaged onto a rectangular grid of 20° latitude–longitude. Although coarse, this grid defines worldwide a large set of potential predictors (see Supplementary Fig. 3) compared with the record length used in the regression computation (53 × 3 months). We therefore combined a predictor selection and an ensemble technique to manage multi-collinearity/overfitting issues and, hence, to enhance the predictive performance of the models (see Supplementary Information).

References

30. Allan, R. & Ansell, T. A new globally complete monthly historical gridded mean sea level pressure dataset (HadSLP2): 1850–2004. *J. Clim.* **19,** 5816–5842 (2006).